ACS OMEGA

http://pubs.acs.org/journal/acsodf

Article

# Facile Synthesis of La- and Chitosan-Doped CaO Nanoparticles and Their Evaluation for Catalytic and Antimicrobial Potential with Molecular Docking Studies

Muhammad Ikram,* Aqib Muhammad Khan, Ali Haider, Junaid Haider, Sadia Naz, Anwar Ul-Hamid,* Anum Shahzadi, Walid Nabgan,* Tahira Shujah, Iram Shahzadi, and Salamat Ali

Cite This: *ACS Omega* 2022, 7, 28459−28470

Read Online

ACCESS | Metrics & More | Article Recommendations

**ABSTRACT:** In the current study, a low-cost and straightforward coprecipitation technique was adopted to synthesize CaO and La-doped CS/CaO NPs. Different weight ratios (2 and 4) of La were doped into fixed amounts of CS and CaO. Synthesized samples exhibited outstanding catalytic performance by degrading methylene blue (MB) in a highly efficient manner. The X-ray diffraction technique detected the presence of a cubic phase of CaO and a decrease in crystallite size of the samples with the addition of La. Fourier transform infrared spectroscopy confirmed the presence of the dopant and the base material with functional groups at 712 $cm^{-1}$. A decrease in the absorption intensity of doped CaO was observed with an increasing amount of dopants La and CS accompanied by a blueshift leading to an increase in the band gap energy from 4.17 to 4.42 eV, as recorded with an ultraviolet−visible spectrophotometer. The presence of dopants (La and CS) and the evaluation of the elemental constitution of Ca and O were supported with the energy-dispersive spectroscopy technique. In an acidic medium, the catalytic activity against the MB dye was reduced (93.8%) for 4% La-doped CS/CaO. For La-doped CS/CaO, vast inhibition domains ranged within 4.15−4.70 and 5.82−8.05 mm against *Escherichia coli* while 4.15−5.20 and 6.65−13.10 mm against *Staphylococcus aureus* (*S. aureus*) at the least and maximum concentrations, correspondingly. In silico molecular docking studies suggested these nanocomposites of chitosan as possible inhibitors against the enoyl-acyl carrier protein reductase (FabI) from *S. aureus*.

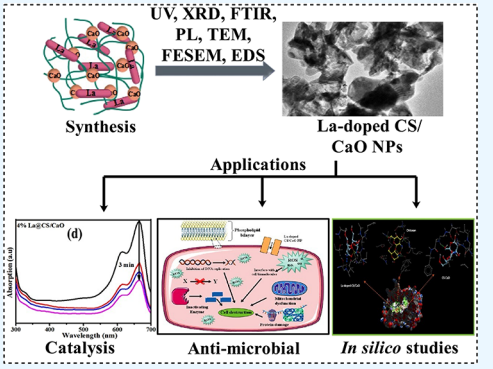




## 1. INTRODUCTION

Industrialization on a large scale increased water contamination due to widespread use of heavy metals and toxic dyes, posing a severe threat to human society and natural ecosystems. The fast expansion of various industrial diverse sectors, such as chemical, leather, medicine, paper, textile, and printing, resulted in the production of toxic metallic ions (Cu, Cr, Pb, and Hg) that pollute the human and aquatic environments with dye toxins.[1,2] Approximately 1/10 of a million distinct types of dyes are generated annually in a diverse range of textile processes. In particular, methylene blue and ciprofloxacin (MBCF) dyes contribute to 10−15% of this pollution as they are being directly dissipated into the environment as effluence. The health of humans and animals is at risk from synthetic dyes and pollutants, which may cause cancer, skin irritability, inflammation, and liver abnormalities.[3]

This alarming situation has shed light on the importance of extracting dyes from wastewater through multiple methods such as the electrochemical process,[4] ultrafiltration membranes,[5] advanced oxidation process,[6] coagulation,[7] and solvent extraction.[8] The catalytic method is recognized as the most energy-efficient, environmentally friendly, and cost-effective[2] for reducing organic dyes[9] with the advantage of recyclability.[10] Furthermore, metal oxide semiconductors (MOs) including CuO, ZnO, MgO, CaO, $CeO_2$, $Fe_3O_4$, and $TiO_2$ have been widely used as catalysts due to their toxic-free nature, low cost, high chemical stability, and activity.[10]

Calcium oxide (CaO) nanoparticles (NPs) have a unique crystalline structure, optical properties, and unusual antimicrobial activity. They are nontoxic and are used as hazardous waste remediation agents and catalysts in several sectors, making the environment safer for all creatures.[11−13] Chitosan (CS) is prepared from the deacetylation of chitin, a polysaccharide biomaterial and the second most abundant

Received: May 20, 2022
Accepted: July 22, 2022
Published: August 2, 2022

biopolymer after cellulose present in insects, lobsters, crabs, crustaceans, and shrimps.[14] Due to the presence of functional groups in its structure, CS exhibits a variety of features, including nontoxicity, biodegradability, and anticancer action.[15] The chelating ability of CS permits interactions with MOs to influence toxic organics, biosensors, and dyes.[16] Chitosan, a hydrophilic polymer containing $NH_2$ and OH side groups, may encompass CaO NPs by hydrogen bonding and generate nanocomposites with novel properties.[17]

The diverse functional groups have strong interactions with the f orbital of lanthanide ions, which allows them to form complexes with Lewis bases (e.g., alcohols, acids, and thiols).[18] Due to the increased surface area and the formation of complexes with lanthanide ions, the concentration of organic contaminants on the surface of semiconductors is elevated. Doping of lanthanide improves catalytic activities and increases the absorption capacity throughout the reaction.[19,20] The La dopant may enhance the stability of the anatase phase by modifying its optical characteristics and inhibiting crystal formation at elevated temperatures.[21] According to the abovementioned detail, we believe that La/CS-doped CaO NPs prepared in this study can act as effective catalysts to remove dyes from polluted water. Furthermore, the preparation of La/CS-doped CaO NPs and their use for the degradation process and antibacterial action have not been studied so far. Therefore, in this research work, undoped CaO and La/CS-doped CaO NPs were prepared using $CaCl_2{\cdot}H_4O_2$, $(C_6H_{11}NO_4)_n$, NaOH, and (2 and 4%) $La(NO_3)_3{\cdot}6H_2O$ through a coprecipitation method. The effect of the dopant La/CS on different characteristics of CaO such as the chemical composition, structure, and antibacterial action was studied. However, the reason behind the usage of these materials is to boost the antibacterial and catalytic activities of the metallic oxides.

## 2. EXPERIMENTAL SECTION

**2.1. Materials and Reagents.** Chitosan $(C_6H_{11}NO_4)_n$, calcium chloride dihydrate ($CaCl_2{\cdot}H_4O_2$, 99%), lanthanum-(III) nitrate hexahydrate ($La(NO_3)_3{\cdot}6H_2O$, 99%), NaOH, 98%, and sulfuric acid ($H_2SO_4$) were acquired from Sigma-Aldrich and Analar.

**2.2. Synthesis of CaO and La/CS-Doped CaO Nanoparticles (NPs).** The synthesis of pure CaO and La/CS-doped CaO NPs through a coprecipitation method was undertaken. A fresh colloidal solution of $CaCl_2{\cdot}H_4O_2$ (0.5 M) was stirred for 20 min, and then, a fixed amount of chitosan (0.5 M) was added into the colloidal stirred solution. Afterward, various concentrations (0.02 and 0.04 wt %) of $La(NO_3)_3{\cdot}6H_2O$ were incorporated into the mixture solution under continual stirring to obtain a homogeneous solution. To maintain the pH at 12, a NaOH (0.5 M) prepared solution was added gradually and stirred for 30 min at 80 °C (Figure 1). A centrifuge machine was used at 7500 rpm for 6 min to separate the obtained product. Finally, samples were dried for 24 h at 100 °C to acquire fine powder. A similar technique was adapted to prepare CaO in the absence of dopants (La and CS).

**2.3. Bacterial Extraction and Identification.** Mastitis-positive caprine milk samples were collected from several livestock clinics and goat farms located in Punjab and swabbed at blood agar (5%). Cultural samples were incubated overnight at 37 °C. Purification of discrete bacteria was accomplished by streaking on MacConkey and mannitol salt agar (MCA and MS) in triplicate. Morphological characterization by Gram staining and biochemical assays as catalase and coagulase tests were adopted to validate standard isolates.

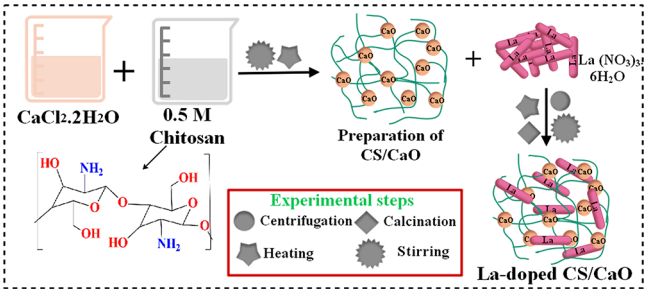


**Figure 1.** Schematic of the synthesis protocol for doped CaO.

**2.4. Bactericidal Evaluation.** In vitro antimicrobial investigation of all samples of concern was performed through a well diffusion technique by culturing $1.5 \times 10^8$ CFU/mL of *S. aureus* and *E. coli* on mannitol salt and MacConkey agar (MS and MCA), separately. Bacterial suspensions were grown onto culture plates with wells of 6 mm diameter created using a sterile cork borer. Different amounts of CaO and La-doped CS/CaO (0.5 and 1.0 mg/50 $\mu$L) were incorporated into each well and differentiated with ciprofloxacin (0.005 mg/50 $\mu$L) and distilled water (50 $\mu$L) as a control positive (+ve) and negative (−ve), separately. Bactericidal viability was surveyed by estimating inhibition regions in millimeter (mm) through a Vernier caliper after loaded Petri dishes were subjected to overnight incubation at 37 °C. Through one-way analysis of variance (ANOVA) using SPSS 23, the microbicidal activity of CaO and La-doped CS/CaO NPs was determined to be remarkable at a 5% significance level.

**2.5. Catalysis.** The catalytic activity of pristine (CaO) and La-doped CS/CaO NPs was evaluated by MB degradation in the presence of sodium borohydride ($NaBH_4$). MB is a cationic thiazine dye that is widely used in analytical chemistry as a redox indicator.[22] In the present experiment, the $NaBH_4$ solution (400 $\mu$L) and sample (doped and undoped, 400 $\mu$L) solution were incorporated in aqueous MB (3 mL) in a quartz cell. The faint blue solution color indicated dye degradation, and MB was reduced to leuco-MB in the company of $NaBH_4$.[23] The observation spectra were captured at various intervals with a UV−visible spectrophotometer at 200 to 700 nm. The mechanism of dye degradation is well-illustrated in Figure 2. $BH_4^-$ donates an electron via CaO and La-doped CS/CaO NPs, which transfers to MB. The most crucial part in dye degradation is played by doped CaO NPs, which accept and then transfer the electron.

**2.6. Molecular Docking Studies.** Keeping in view the good bactericidal potential of chitosan and its nanocomposites (i.e., CS/CaO and La-doped CS/CaO) against Gram −ve and Gram +ve strains, we evaluated their binding potential through molecular docking studies against the enoyl-acyl carrier protein reductase enzyme (FabI) from *E. coli* as well as *S. aureus*. The selection of the enzyme was based on the fact that FabI is a target of the kalimantacin class of antibiotics that are effective in the treatment of multidrug-resistant *S. aureus*. Crystal structures (i.e., 3D coordinates) were retrieved from a repository of protein structures. The accession code for $FabI_{E.\ coli}$ and $FabI_{S.\ aureus}$ are 1MFP (res: 2.3 Å) and 6TBC (res: 2.5 Å),[24,25] respectively.

ICM version 3.8-7d (Molsoft LLC, La Jolla, CA) was employed for molecular docking predictions.[26] A previously


https://doi.org/10.1021/acsomega.2c02790
ACS Omega 2022, 7, 28459−28470

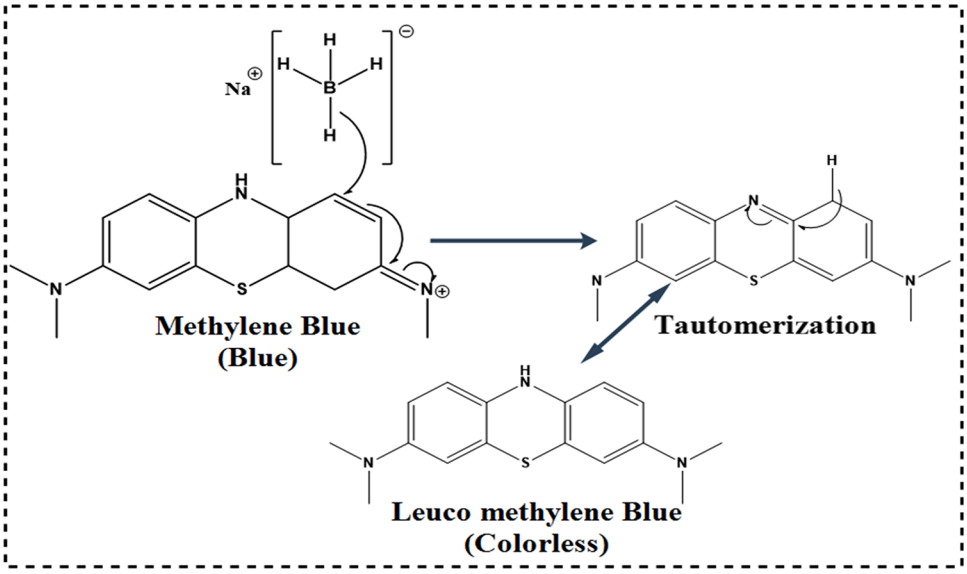


**Figure 2.** Schematic diagram illustrating the mechanism of catalysis.

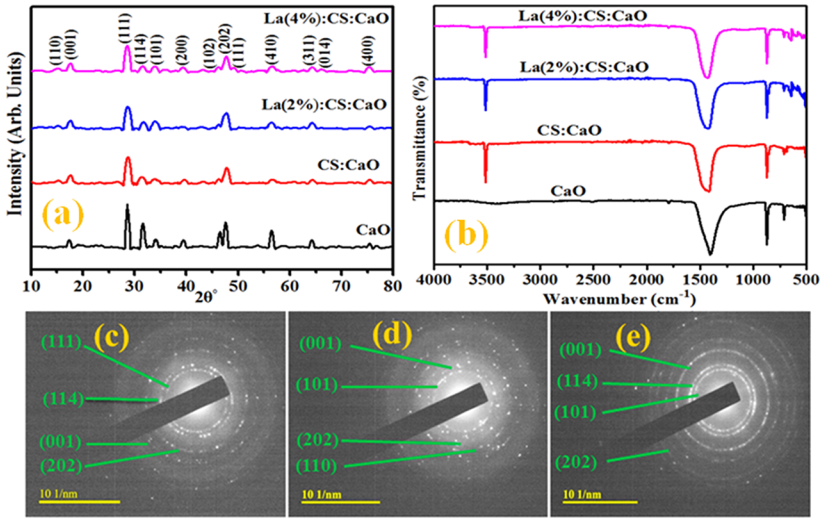


**Figure 3.** (a) XRD analysis, (b) FTIR results of doped CaO, and (c−e) SAED patterns of synthesized products.

reported standard method for protein structure preparation involved energy minimization (using a default force field), H atom as well as Gasteiger charge addition, and native ligand and $H_2O$ molecule removal. The optimized protein structures were then subjected to molecular docking studies where a binding pocket was specified around a native ligand (within a 5 Å distance). The three-dimensional (3D) structures of nanocomposites were built by modification of the chitosan structure obtained from PubChem. Ligand structure preparation was accomplished through the ligedit tool of ICM, and the best conformation was generated for each nanocomposite using a conformational analysis tool and finally optimized. The top 10 docked conformations were generated in each case to get the best docked complex for further analysis.

**2.7. Scavenging (DPPH Assay).** All specimens' free radical scavenging efficiency was determined using a modified version of the traditional DPPH scavenging assay. Various amounts of pure CaO, CS/CaO, 2% La-CS/CaO, and 4% La-CS/CaO nanomaterials (50−300 $\mu$g/mL) were produced and combined with an equivalent volume of a 0.1 mM DPPH reagent. The reaction mixture was vortexed and incubated for 30 min at room temperature in the dark. Ascorbic acid was used as the control antioxidant. A spectrophotometer was used to determine the mixture's absorbance at 517 nm. The percent scavenging ability was estimated using the following equation:

$$\text{DPPH scavenging rate}(\%) = (A_0 - A_1) \times 100A_0$$

where $A_0$ represents the absorbance of the control solution (methanol + DPPH) and $A_1$ represents the absorbance of the sample.

**2.8. Characterization.** The structure and crystalline features of synthesized powders were assessed through an X-ray diffractometer (model: PANalytical X'Pert PRO) using Cu K$\alpha$ radiation ($\lambda$ = 1.540 Å) and 2$\theta$ values from 10 to 80°. A functional group study was carried out through an FTIR spectrometer (PerkinElmer) used in the 4000−500 cm$^{-1}$ range. Optical properties were investigated with a UV−vis spectrophotometer (Genesys 10S) in the 200−700 nm range, while using a spectrofluorometer (JASCO, FP-8300), photoluminescence (PL) spectroscopy was performed. The


https://doi.org/10.1021/acsomega.2c02790
ACS Omega 2022, 7, 28459−28470

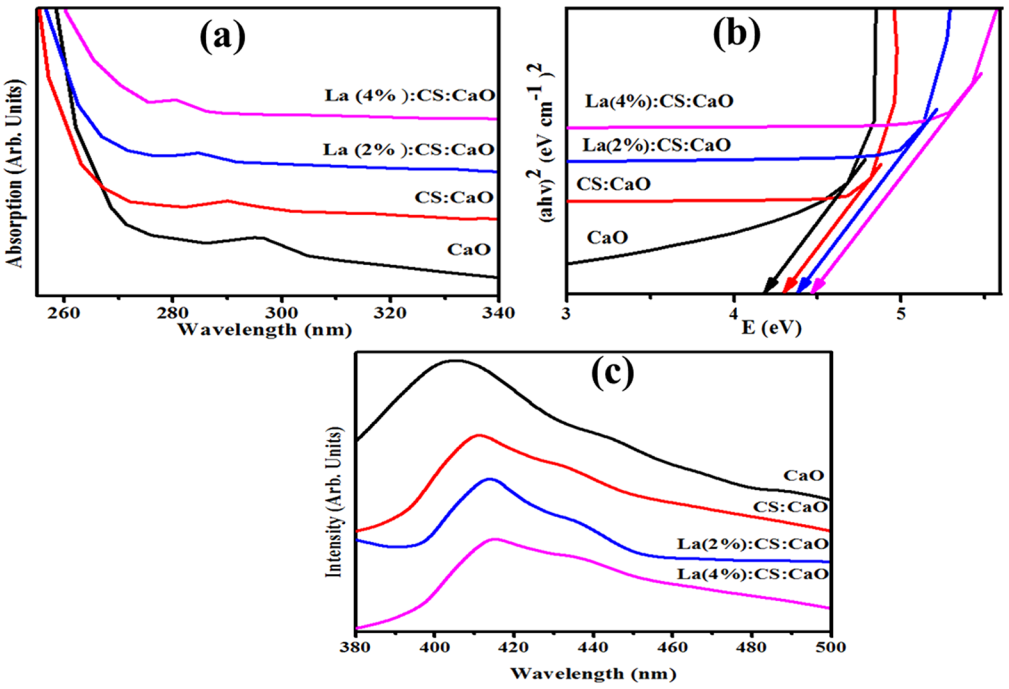


**Figure 4.** (a) UV/visible absorption spectra, (b) $E_g$ graph, and (c) PL spectra.

elemental composition was attained via SEM−EDS using INCA EDS software.

## 3. RESULTS AND DISCUSSION

For the crystal structure and phase formation of undoped and codoped CaO NPs, X-ray diffraction (XRD) has been used ranging from 10 to 80° (Figure 3a). The observed diffraction peaks at $2\theta$ = 28.6, 31.5, 39.5, 47.5, 56.6, 64.2, and 75.3° are attributed to the (111), (114), (200), (202), (410), (311), and (400) planes, which confirmed the cubic phase of CaO (JCPDS card no. 00-037-1497, ICDD card no. 00-017-0912, and JCPDS file no. 37-1497). XRD patterns also show some intense peaks at 17.8, 34.1, and 46.5°, corresponding to the (001), (101), and (102) orientation planes, respectively, being referred toward the presence of $Ca(OH)_2$ (JCPDS card number 44-1481). The sample was subjected to air humidity, resulting in the $Ca(OH)_2$ phase.[27] The characteristics peak of CS appeared at 15.2° (110), which confirms successful doping in CaO NPs.[28] XRD patterns of La 2% exhibit the same generation of peaks due to the low La content. Meanwhile, upon higher doping (4%), two additional peaks at 48.8 and 66° corresponding to the (111) and (014) crystal faces were observed. These peaks confirm the doping of La into CaO, which appeared mainly in the form of lanthanum oxide ($La_2O_3$) with JCPDS card no. 73-2141. The average crystallite size of prepared catalysts was calculated using Debye−Scherrer's formula. Computed crystallite sizes are 34.2, 32.3, 30.7, and 29.5 nm for CaO, CaO-CS, and La (2 and 4%)/CaO-CS, respectively. The crystallite size of prepared NPs decreased upon doping with La, which corresponds to an increase in FWHM values. The crystallite size of prepared NPs decreased on La doping as lanthanum has a higher ionic radius than calcium. Consequently, the incorporation of $La^{+3}$ creates oxygen vacancies, which may help to change the La−O bond causing reduction in crystallite size.[29]

FTIR was used to analyze the transmission spectrum of prepared samples using infrared radiation. Functional group assessment in prepared samples was carried out relative to the position of vibrational peaks in FTIR spectra. Figure 3b shows peaks at 1400 and 877 $cm^{-1}$ corresponding to the C−O bond associated with the carbonation of CaO nanostructures. The band at 712 $cm^{-1}$ specifies the Ca−O bonds confirming the CaO NP formation. The bands at 2509 and 1793 $cm^{-1}$ are attributed to O−H groups and C═O bonds, respectively.[30,31] The peak found around 3429 $cm^{-1}$ in the spectra is also evidence of the OH stretching vibration.[13] Meanwhile, the chitosan peak appearing at 3500 $cm^{-1}$ corresponds to the amine ($-NH_2$) functional group. This functional group in the chitosan chain serves as a coordination and reaction site for the adsorption of organic species.[31,32] A spike found at ∼650 $cm^{-1}$ is attributed to the La−O bond.[33] A change in peak intensity ascertains substitution of La/CS in CaO nanostructures successfully. Furthermore, the dotted concentric rings observed from SAED confirm the crystalline nature of CaO, Ch-CaO, and 4% doped CaO (Figure 3c−e).

The absorption spectra of dispersed nanocomposite solutions in water had been measured using a UV−vis spectrophotometer at ambient temperature (Figure 4a). The maximum absorption peak of CaO was observed at ∼297 nm,[34] while CS/CaO peaks were recorded at 290 nm in the UV spectra. CaO is formed when two Ca 4s electrons are transported to the O 2p orbital, resulting in the generation of the $Ca^{2+}$ and $O^{2-}$ ions.[35] La-doped (2 and 4%) CS/CaO absorption peaks were found around 275−288 nm. Furthermore, quantum confinement may result in a wavelength decrease toward the lower energy upon incorporation of the La dopant.[36] Band gap energies ($E_g$) were calculated using the Tauc equation, and the corresponding graph was plotted for $(\alpha h\upsilon)^2$ vs photon energy. The $E_g$ value for CaO was found to be 4.17.[34] On increasing the dopant concentration, the $E_g$ increased for CS/CaO and 2 and 4% La-doped CS/CaO to 4.27, 4.35, and 4.42 eV, respectively (Figure 4b).

Photoluminescence spectroscopy (PL) of samples of concern was carried out to analyze the electron−hole pair


https://doi.org/10.1021/acsomega.2c02790
ACS Omega 2022, 7, 28459−28470

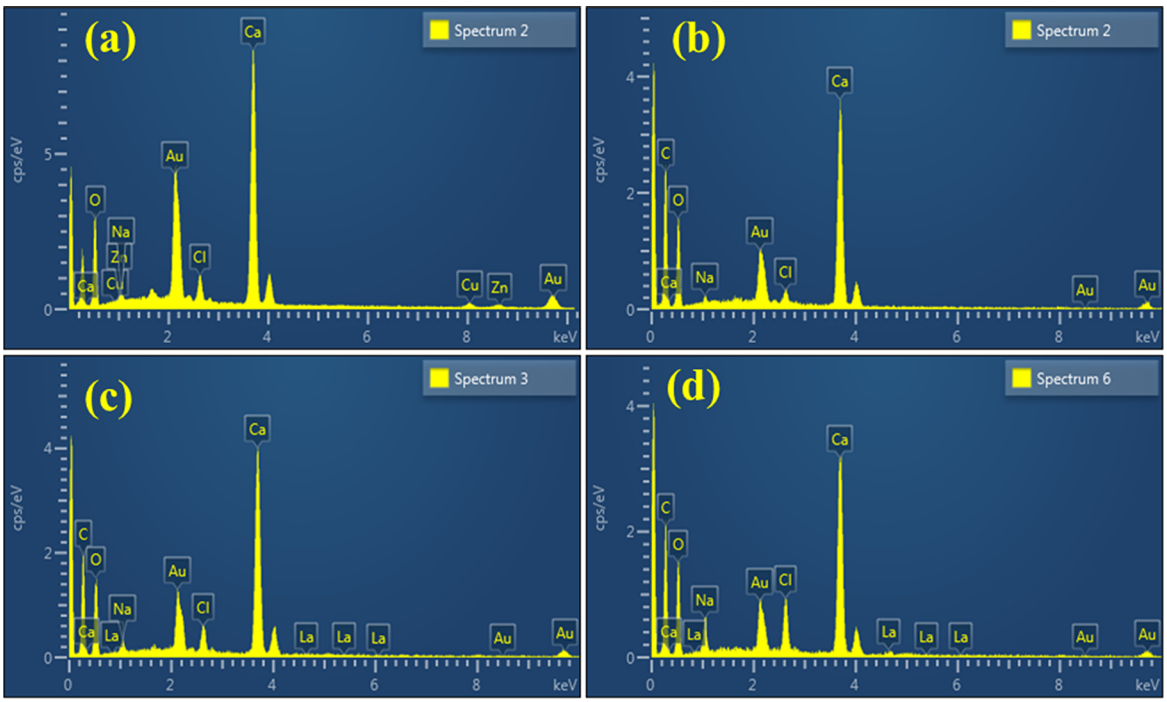


**Figure 5.** EDS analysis of La-doped CS/CaO (a–d).

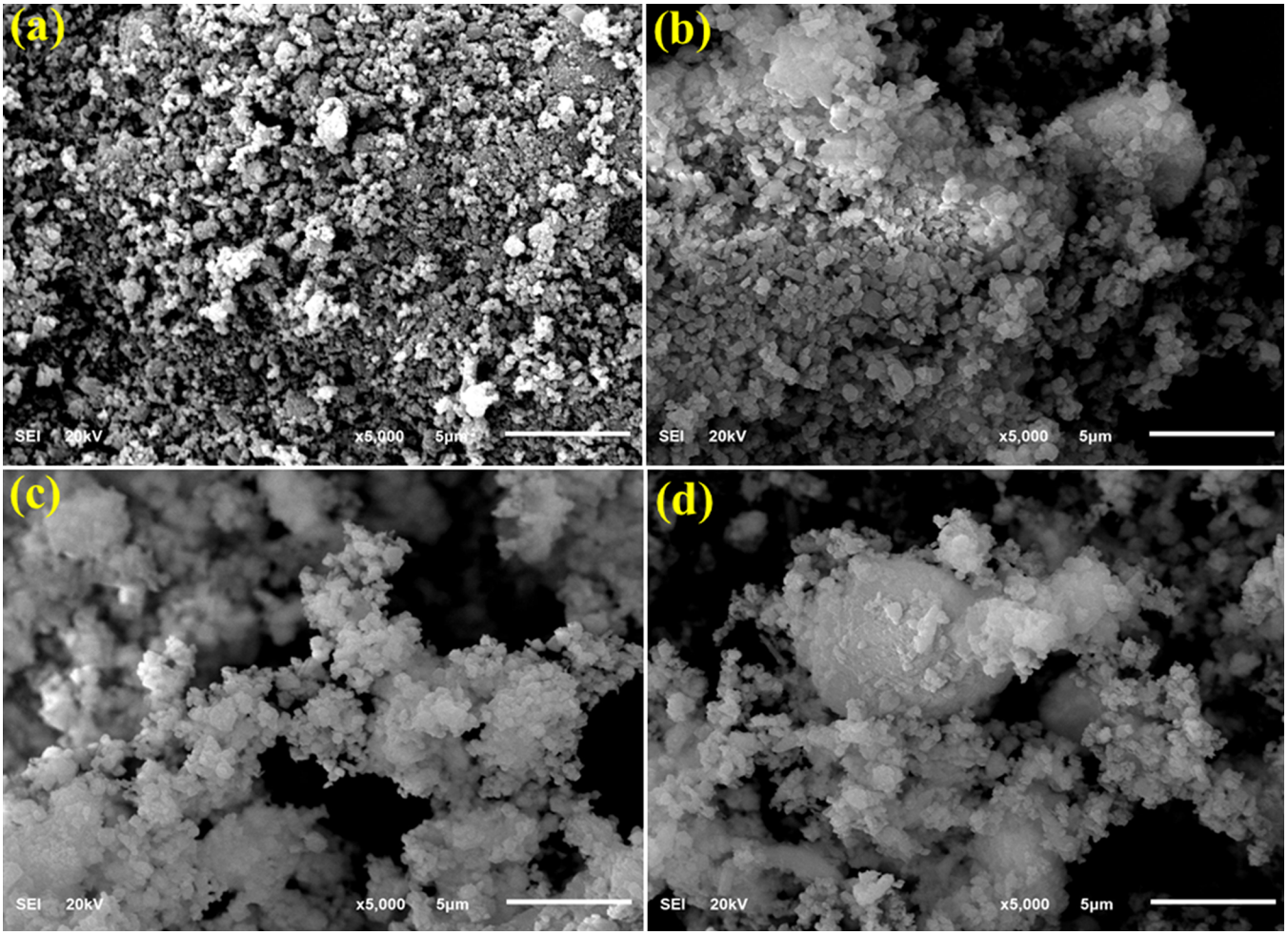


**Figure 6.** (a–d) SEM images of CaO and La-doped CS/CaO.



https://doi.org/10.1021/acsomega.2c02790
*ACS Omega* 2022, 7, 28459–28470

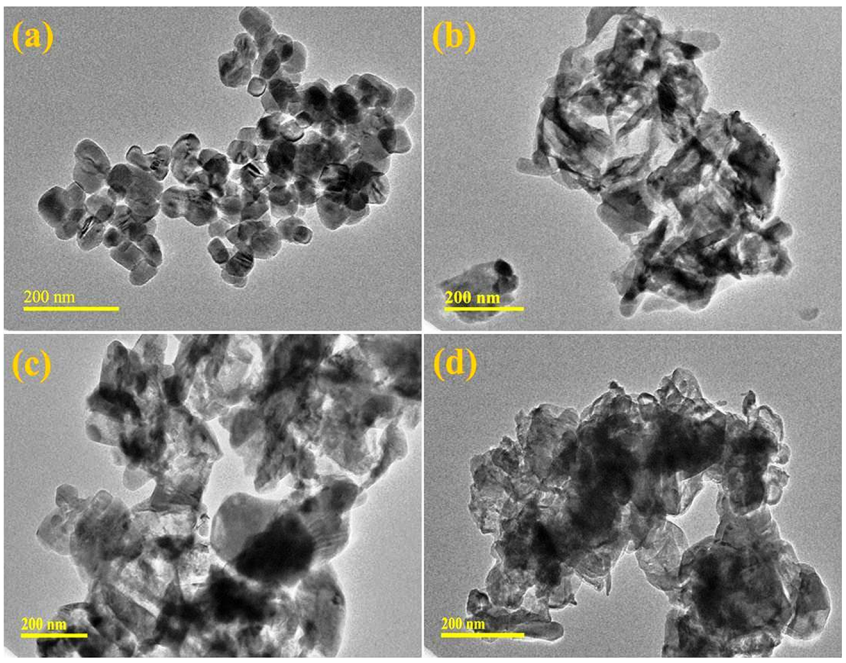


**Figure 7.** (a–d) TEM images of synthesized CaO, CS/CaO, and La (2%)- and (4%)-doped CS/CaO.

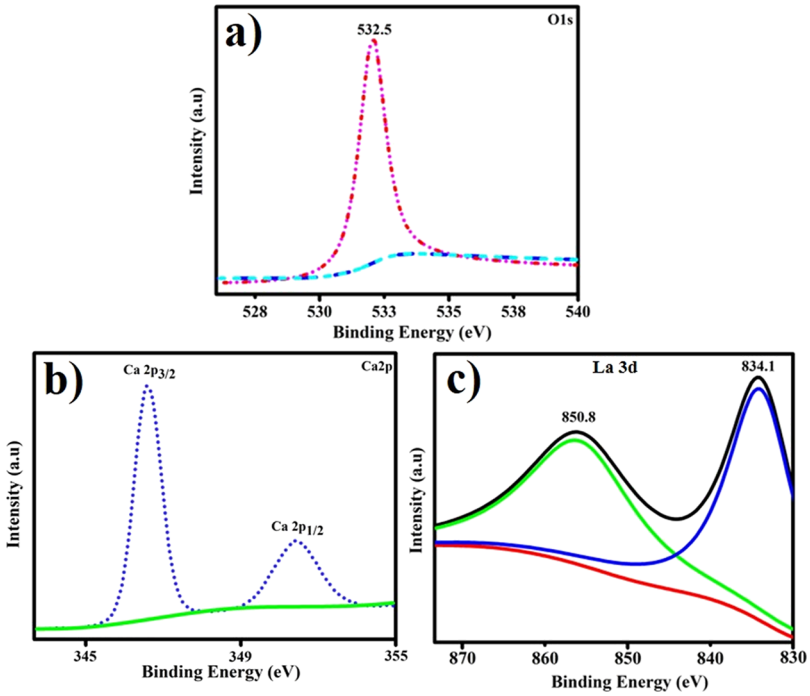


**Figure 8.** XPS spectra of CaO: (a) O 1s, (b) Ca 2p, and (c) and La 3d.

recombination and dynamic separation.[37] Generally, the rate of electron–hole pair recombination varies with PL intensity, where a low peak intensity has low recombination of electron–hole pairs. The catalytic activity of nanomaterials increases as PL intensity decreases.[38,39] Figure 4c shows emission spectra of the control and La-doped CS/CaO in the range of 380 to 500 nm with an excitation wavelength of 300 nm. The emission peak of CaO NPs was located at 405 nm, which might originate from the charge recombination and intrinsic defects.[27] Meanwhile, the CS/CaO emission peak was observed at 411 nm in the PL spectra. Afterward, upon La doping, the position of UV emission bands increased (405 to 415 nm) compared to the pristine sample. In UV emission spectra, the redshift may be due to the strain created in the crystal lattice to accommodate large La atoms in CaO.[40]

EDS spectroscopy was performed to identify the chemical composition of CaO and La-doped CS/CaO NPs. The EDS spectrum (Figure 5a) exhibits the Ca and O peaks, which confirms the NP formation. The peaks of C and La in the spectra (Figure 5b–d) show the successful doping of CS and La into CaO. Meanwhile, the peak of Na observed for all synthesized samples was mainly due to NaOH solution used to retain the pH of samples of concern. The presence of extra



https://doi.org/10.1021/acsomega.2c02790
ACS Omega 2022, 7, 28459–28470

**Table 1. In Vitro Bactericidal Performance of CaO and La-Doped CS/CaO**

| | inhibition region (mm)[a] | | inhibition region (mm)[b] | |
|---|---|---|---|---|
| samples | 0.5 mg/50 μL | 1.0 mg/50 μL | 0.5 mg/50 μL | 1.0 mg/50 μL |
| CaO | 1.90 | 3.30 | 1.90 | 2.25 |
| CS:CaO | 4.15 | 5.82 | 4.15 | 6.65 |
| La (2%):CS:CaO | 4.55 | 6.65 | 4.80 | 10.05 |
| La (4%):CS:CaO | 4.70 | 8.05 | 5.20 | 13.10 |
| ciprofloxacin | 7.15 | 7.15 | 9.20 | 9.20 |
| DIW | 0 | 0 | 0 | 0 |

[a]Inhibition region values for G −ve. [b]Inhibition areas (mm) for G +ve.

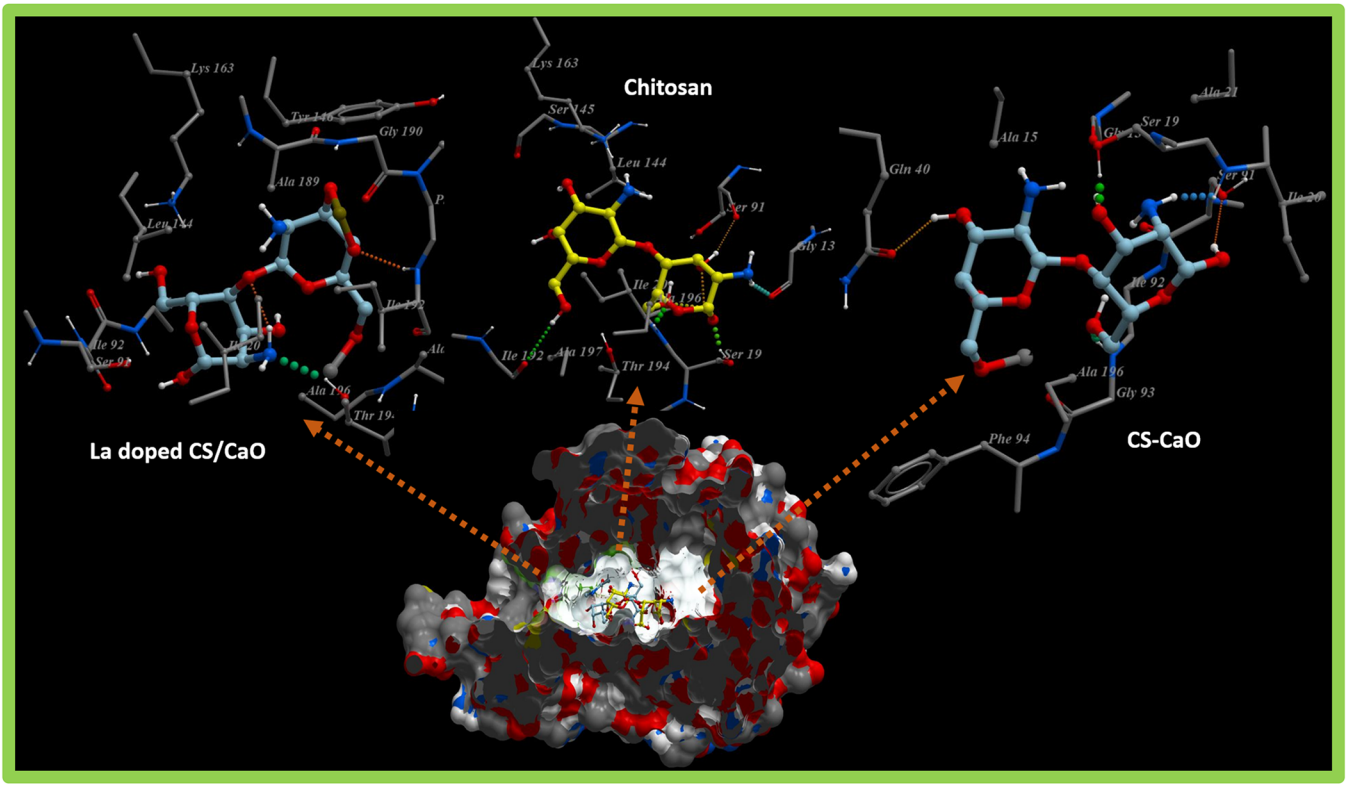


**Figure 9.** 3D graphical representation of binding interaction patterns of chitosan, chitosan-Ca, and chitosan-Ca/La nanocomposites inside active pockets of FabI from *E. coli* ($FabI_{E.\ coli}$).

elements (Au and Cl) may also be attributed to the high background count in the EDS detector.

FESEM was utilized to identify the prepared samples' surface morphology with negatively charged electrons (Figure 6a−d). The FESEM image of CaO (Figure 6a) shows the aggregation of particles distributed nonuniformally. The incorporation of CS into CaO (Figure 6b) revealed overlapping of CS with CaO agglomeration. Afterward, the addition of a small concentration of La to CS/CaO indicated the agglomeration without identification of La (Figure 6c). This agglomeration increases with an increasing amount of La in the host material (Figure 6d).

TEM was carried out to study the topography and morphological formation of CaO and doped CaO NPs (Figure 7a−d). The TEM image of CaO prepared through the coprecipitation method (Figure 7a) confirms the presence of the aggregated cubic phase of NPs as described in the XRD analysis of CaO. This aggregation can be attributed to hydrogen bonding of the solvent (DI water). The addition of CS into CaO (Figure 7b) showed a CS rod-like polymeric network overlapping with the host material. Doping of La (2%, Figure 7c) showed that a combination of nanorods and the cubic phase of NPs results in aggregation. A higher concentration of La into the host material revealed the high agglomeration of nanorods and cubic NPs revealing the formation of a network due to the presence of CS (Figure 7d). Particle sizes of prepared NPs were calculated through TEM images by using ImageJ software. Calculated particle sizes are 37.3, 36.5, 35, and 34.3 nm for CaO, CaO-CS, and La (2 and 4%)/CaO-CS, respectively. The particle size decreased because particles are agglomerated as concentrations of dopants were increased.

The compositional framework and phase purity of the elements were determined by examining the XPS spectra of La-doped CS/CaO NPs. Figure 8a−c depicts the narrow-scan XPS spectra of CaO O 1s, Ca 2p, and La 3d of the produced materials. The composite CaO O 1s signal exhibits a peak at 532.5 eV, which corresponds to the C−O bond in Figure 8a.[41] As illustrated in Figure 8b, the two high peaks at 346.5 and 351.2 eV correspond to Ca $2p_{3/2}$ and Ca $2p_{1/2}$ in CaO.[42]



https://doi.org/10.1021/acsomega.2c02790
ACS Omega 2022, 7, 28459−28470

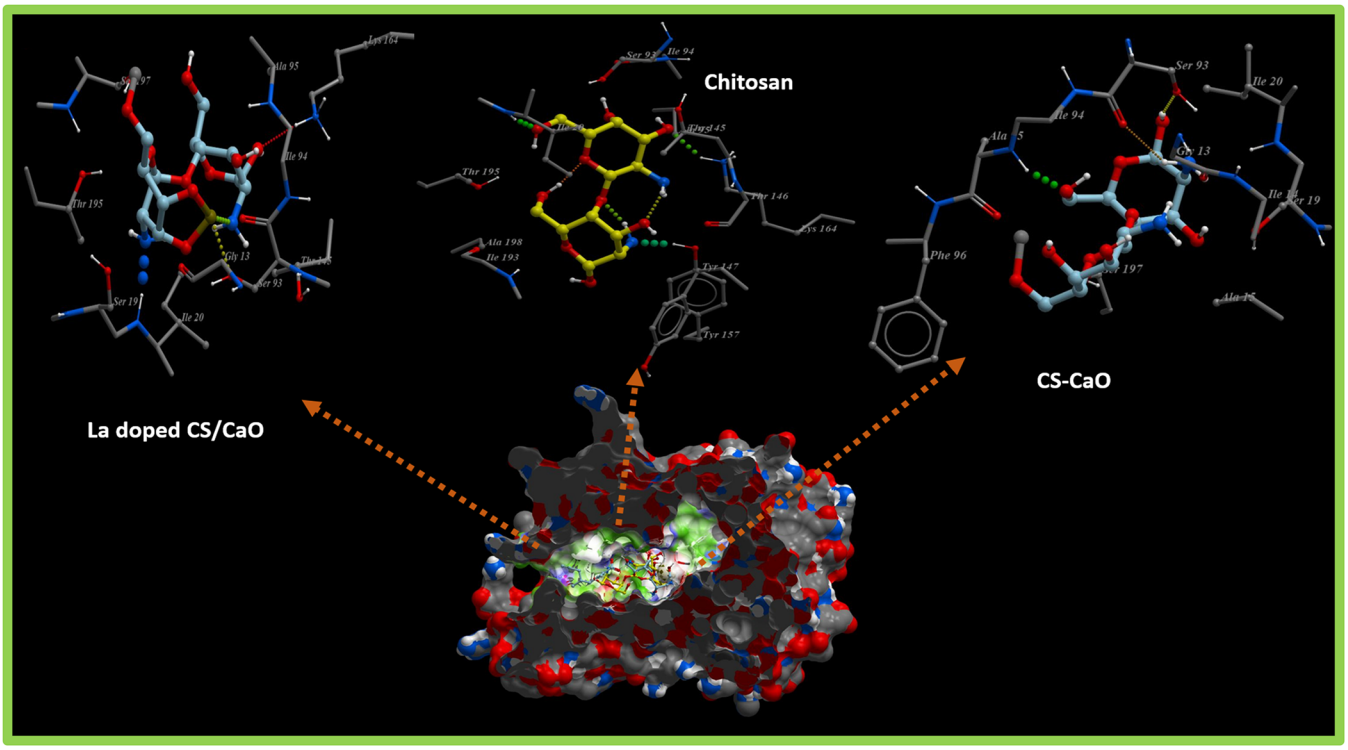


**Figure 10.** 3D graphical representation of binding interaction patterns of chitosan, chitosan-Ca, and chitosan-Ca/La nanocomposites inside active pockets of FabI from *S. aureus* ($FabI_{S.\ aureus}$).

Figure 8c depicts the binding energy spectra in the La $3d_{5/2}$ region for the codoped CaO NPs. The La $3d_{3/2}$ and $3d_{5/2}$ core levels are detected in this diagram to be around 850.8 and 834.1 eV, correspondingly.[43]

The in vitro microbicidal expression of CaO and La-doped CS/CaO NPs was monitored by comparing inhibition ranges (mm) using a well diffusion approach toward *E. coli* and *S. aureus* (Table 1). The measurements have been shown to be synergistic with the concentration and formed domains of inhibition (mm). CaO depicted 1.90 and 3.30 mm inhibition regions for G −ve and, similarly, 1.90 and 2.25 mm for G +ve at the least and maximum concentrations, correspondingly. For La-doped CS/CaO, vast inhibition domains ranged within 4.15−4.70 and 5.82−8.05 nm against *E. coli* while 4.15−5.20 and 6.65−13.10 nm against *S. aureus* at both concentrations, separately. Ciprofloxacin exhibited inhabitation ranges of 7.15 and 9.20 nm targeting *E. coli* and *S. aureus*, separately, in comparison to distilled water (0 mm). At a high dose, La (4%) showed substantial ($p < 0.05$) bactericidal action for G +ve in contrast to G −ve.

The dimension, shape, and mass-to-surface ratios of manufactured doped NPs are all dependent on oxidative stress since tiny particles quickly release reactive oxygen species (ROS), which degrade the cytoplasmic constituents of bacteria, ending in their collapse .[44,45] The increased concentration of NPs after contact resulted in enhanced antibacterial activities. The considerable increase in antibacterial activity of doped NPs is a result of the synergistic impact created by the coexistence of both metallic species.[46] Another mechanism through which nanoparticles engage with microbes is by robust cationic contact with negatively charged microbial constituents, resulting in the collapse of bacteria.[47,48]

The fatty acid biosynthetic pathway plays a pivotal role in the survival of bacteria and has been reported as a target of various antibiotics discovered previously. Enzymes belonging to the fatty acid biosynthetic pathway, particularly the enoyl-acyl carrier protein reductase enzyme (FabI), have huge therapeutic importance and have been reported as promising targets for antibiotic discovery.[49,50] Here, molecular docking studies of chitosan, chitosan-Ca, and chitosan-Ca/La nanocomposites revealed their potential as possible inhibitors of the enoyl-acyl carrier protein reductase enzyme (FabI). The binding patterns observed for all these nanocomposites inside active pockets of $FabI_{E.\ coli}$ and $FabI_{S.\ aureus}$ are presented in Figures 9 and 10, respectively.

For the case of $FabI_{E.\ coli}$, chitosan showed H-bond interactions with Thr194 (2.9 Å), Ile192 (3.4 Å), Lys163 (3.1 Å), Ile20 (2.7 Å), and Ser91 (2.8 Å) alongside hydrophobic interactions with Leu144 and Ala196 having a binding score of −11.930 kcal/mol. Similarly, chitosan-Ca and chitosan-Ca/La nanocomposites also showed comparable binding interactions and scores with active site residues as shown in Figure 9. In the case of chitosan-Ca, residues interacting through H-bonds were Gln40 (2.9 Å), Gly93 (2.6), and Ser91 (2.7 Å), while Gly13, Ile20, and Ala196 showed hydrophobic interactions with active pockets having an overall binding score of −9.917 kcal/mol. Furthermore, chitosan-Ca/La (binding score of −10.037 kcal/mol) interacted through H-bonds with Ile94 (2.8 Å) and Thr194 (3.3 Å) of active pockets and hydrophobic interactions with Ile20, Ser91, Gly93, and Leu144 as depicted in Figure 9. Chitosan and its nanocomposites showed similar trends of binding against active sites of $FabI_{S.\ aureus}$, i.e., an attractive target for antistaphylococcal agents.

Chitosan showed H-bonds with Ile20 (3.0 Å), Lys164 (3.0 Å), Thr195 (2.8 Å), and Tyr157 (3.1 Å), while hydrophobic bonds were observed for Ser93, Thr145, and Tyr147 (binding score of −8.828 kcal/mol) as shown in Figure 10. Both


https://doi.org/10.1021/acsomega.2c02790
ACS Omega 2022, 7, 28459−28470

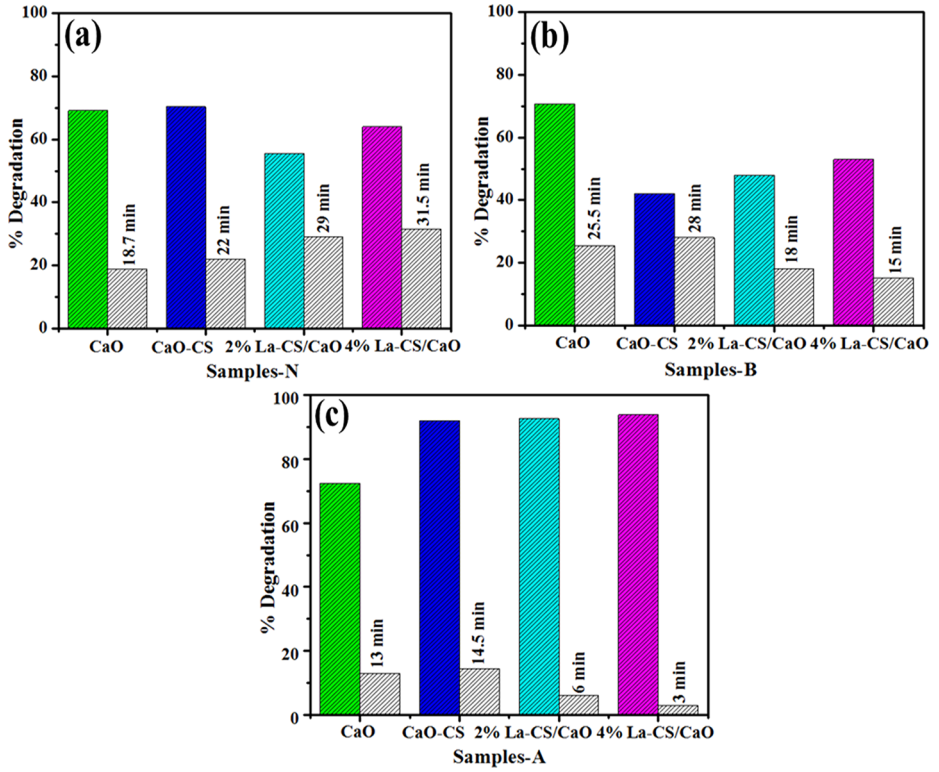


**Figure 11.** Catalysis of CaO, CS:CS, and La (2 and 4%):CS:CaO in different media: (a) neutral, (b) basic, and (c) acidic with different time intervals.

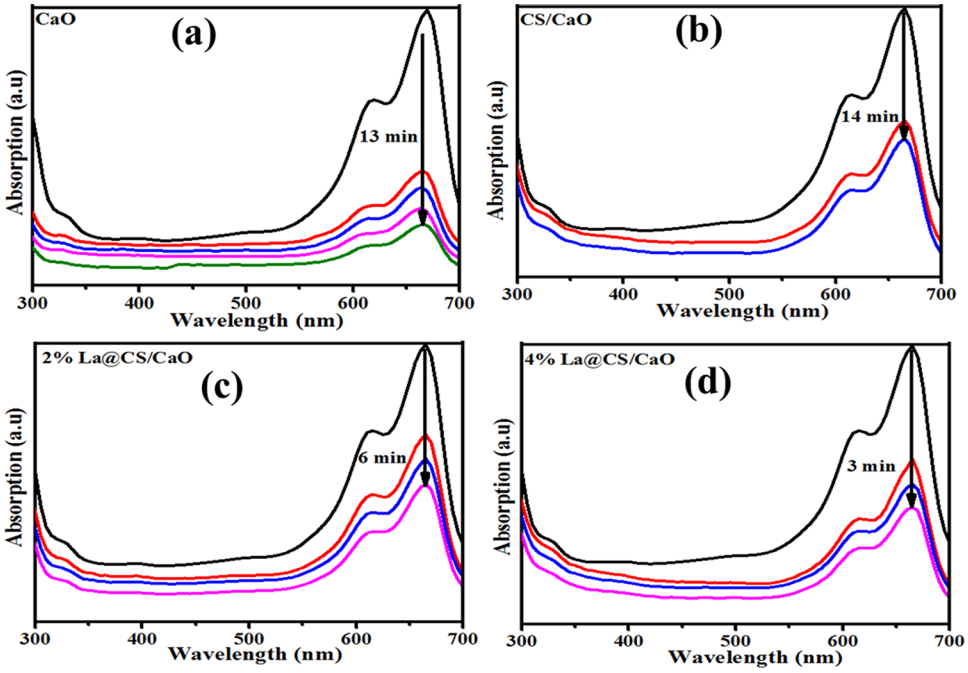


**Figure 12.** (a–d) MB absorption peaks for acidic medium.

chitosan-Ca (−7.793 kcal/mol) and chitosan-Ca/La (−7.148 kcal/mol) nanocomposites showed H-bonds with Ser93 (2.8 and 2.3 Å) and hydrophobic interactions with Ser19, whereas other H-bonds were observed with Ala95 (1.4 Å) for the chitosan-Ca nanocomposite and with Ile20 (2.9 Å) and Lys164 (3.0 Å) for chitosan-Ca/La nanocomposites as evident from Figure 10.

UV–visible absorption spectra were obtained upon the reference sample, and dye degradation (MB) was used to test the catalytic performance of dopant-free and La-doped CS/CaO NPs. At neutral conditions (pH = 7), $NaBH_4$ (400 $\mu$L) was added into MB (3 mL), and 3 mL of the sample showed dye degradation of 69.07, 70.3, 55.5, and 63.95% for undoped and doped samples. Meanwhile, the basic solution (pH = 12) indicates degradation of 70.64, 42, 58, and 53%. Moreover, the



https://doi.org/10.1021/acsomega.2c02790
ACS Omega 2022, 7, 28459−28470

acidic medium (pH = 4) shows 72.48, 91.97, 92.63, and 93.88% dye degradation as shown in Figure 11a–c. Pure CaO shows above 65% dye degradation in all media; upon doping, degradation decreases in basic medium as compared to neutral. This finding proves that maximum dye degradation was achieved in an acidic medium upon doping of CS and La (2 and 4%), as depicted in Figure 11c. Increased generation of $H^+$ ions available for adsorption on the nanostructure surface increases the catalytic activity in acidic media. The quantity of hydroxyl groups rises in basic media, reducing product oxidation and catalytic activity. The catalytic activity depends on the nanomaterials' surface area, morphology, and crystallinity.[3] During catalysis, the synthesized material caused dye reduction upon electron transfer from $BH_4^-$ ions (donor) to MB (acceptor).[51] The pH and dyes are also influential factors for wastewater treatment. The highest dye (MB) degradation was acquired in acidic medium by using the materials of concern. Figure 12a–d shows that degradation of MB occurs at a wavelength of 665 nm for CaO, CS/CaO, and (2 and 4%) La-doped CS/CaO NPs for acidic medium.

Scavenging (DPPH) tests for pristine CaO, CS/CaO, 2% La-CS/CaO, and 4% La-CS/CaO nanomaterials were performed to investigate the active radical species present in the photocatalyst and to determine their antioxidant activity. Antioxidant properties of substances determined their capacity to donate electrons or hydrogen atoms to the DPPH free radical, forming stable diamagnetic compounds. The capacity of this DPPH free radical to reduce might be determined spectrophotometrically by measuring the decrease in absorbance at 517 nm. It was observed in this investigation that the nanoparticles' DPPH activity increased dose-dependently (Figure 13). It is verified that pristine CaO had strong

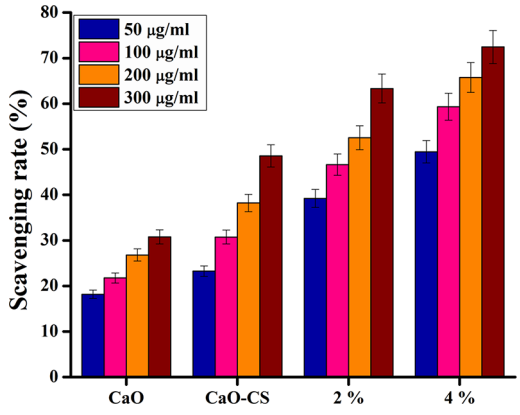


**Figure 13.** DPPH radical scavenging potential of CaO, CS/CaO, 2% La-CS/CaO, and 4% La-CS/CaO nanomaterials.

scavenging activity (30.77%) and may generate reactive oxygen species as OH·, $O_2^{\cdot-}$, and $^1O_2$, which can interact with the DPPH free radical.[52,53] According to recent research, $^1O_2$ is the primary active species in the degradation of the MB dye when exposed to sun radiation.[54] However, increasing the concentration of the doped material, the scavenging activity increases, and the highest increase in scavenging activity is noted for 4% La-CS/CaO (72.44%).

## 4. CONCLUSIONS

La-doped CS/CaO NPs were successfully synthesized using a coprecipitation technique with different La dopant concentrations (2 and 4%). According to the experimental results, XRD analysis confirmed the cubic phase of CaO, and the calculated crystallite size of the prepared samples decreased from 34.2 to 29.5 nm with an increasing amount of the dopant. FTIR spectroscopy analyzed the functional groups, and the characteristic peak of CaO was observed at ∼712 $cm^{-1}$. An increase in band gap energy from 4.17 to 4.42 eV was revealed accompanied by a blueshift in absorption upon CS and La doping. PL analysis indicated a redshift and confirmed the effect of doping. In addition, the EDS technique confirmed the elemental composition and successful doping of La and CS. The highest dye degradation, about 93.8%, was achieved in an acidic medium by 4% La doping in CS/CaO NPs. Overall, at a high concentration, La (4%) evidenced substantial bactericidal action for G +ve compared to G −ve indicating La-doped CS/CaO NPs as potential antibacterial agents in future medicine. In silico molecular docking studies suggested these nanocomposites of chitosan as potential inhibitors against $FabI_{S.\ aureus}$ that may provide new insight into the role of nanomaterials as possible antistaphylococcal agents.

## AUTHOR INFORMATION


### Corresponding Authors

**Muhammad Ikram** − *Solar Cell Applications Research Lab, Department of Physics, Government College University Lahore, Lahore 54000 Punjab, Pakistan;* orcid.org/0000-0001-7741-789X; Email: dr.muhammadikram@gcu.edu.pk

**Anwar Ul-Hamid** − *Core Research Facilities, Research Institute, King Fahd University of Petroleum & Minerals, Dhahran 31261, Saudi Arabia;* orcid.org/0000-0002-0259-301X; Email: anwar@kfupm.edu.sa

**Walid Nabgan** − *Departament d'Enginyeria Química, Universitat Rovira i Virgili, 43007 Tarragona, Spain;* Email: walid.nabgan@urv.cat

### Authors

**Aqib Muhammad Khan** − *Department of Physics, Riphah Institute of Computing and Applied Sciences (RICAS), Riphah International University, Lahore 54000, Pakistan*

**Ali Haider** − *Faculty of Veterinary and Animal Sciences, Muhammad Nawaz Shareef University of Agriculture, Multan 66000, Pakistan*

**Junaid Haider** − *Tianjin Institute of Industrial Biotechnology, Chinese Academy of Sciences, Tianjin 300308, China*

**Sadia Naz** − *Tianjin Institute of Industrial Biotechnology, Chinese Academy of Sciences, Tianjin 300308, China*

**Anum Shahzadi** − *Faculty of Pharmacy, The University of Lahore, Lahore 54000, Pakistan*

**Tahira Shujah** − *Department of Physics, University of Central Punjab, Lahore 54000, Pakistan*

**Iram Shahzadi** − *Punjab University College of Pharmacy, University of the Punjab, Lahore 54000 Punjab, Pakistan*

**Salamat Ali** − *Department of Physics, Riphah Institute of Computing and Applied Sciences (RICAS), Riphah International University, Lahore 54000, Pakistan*

Complete contact information is available at: https://pubs.acs.org/10.1021/acsomega.2c02790


### Notes

The authors declare no competing financial interest.



https://doi.org/10.1021/acsomega.2c02790
ACS Omega 2022, 7, 28459−28470

## ■ ACKNOWLEDGMENTS

The authors are thankful to KFUPM, Saudi Arabia, for support in the morphological study and HEC, Pakistan, through NRPU 20-17615.

## ■ REFERENCES

(1) Jiao, M.; Yao, Y.; Chen, C.; Jiang, B.; Pastel, G.; Lin, Z.; Wu, Q.; Cui, M.; He, S.; Hu, L. Highly Efficient Water Treatment via a Wood-Based and Reusable Filter. *ACS Materials Lett.* **2020**, *2*, 430−437.

(2) Hassan, J.; Ikram, M.; Ul-Hamid, A.; Imran, M.; Aqeel, M.; Ali, S. Application of Chemically Exfoliated Boron Nitride Nanosheets Doped with Co to Remove Organic Pollutants Rapidly from Textile Water. *Nanoscale Res. Lett.* **2020**, *15*, 2777.

(3) Ikram, M.; Hayat, S.; Imran, M.; Haider, A.; Naz, S.; Ul-Hamid, A.; Shahzadi, I.; Haider, J.; Shahzadi, A.; Nabgan, W.; Ali, S. Novel Ag/Cellulose-Doped $CeO_2$ Quantum Dots for Efficient Dye Degradation and Bactericidal Activity with Molecular Docking Study. *Carbohydr. Polym.* **2021**, *269*, No. 118346.

(4) Radjenovic, J.; Sedlak, D. L. Challenges and Opportunities for Electrochemical Processes as Next-Generation Technologies for the Treatment of Contaminated Water. *Environ. Sci. Technol.* **2015**, *49*, 11292−11302.

(5) Jessup, A. Photocatalytic Antifouling PVDF Ultrafiltration Membranes Based on Synergy of Graphene Oxide and $TiO_2$ for Water Treatment. *J. Membr. Sci.* **2013**, *8*, 71−76.

(6) Andreozzi, R.; Caprio, V.; Insola, A.; Marotta, R. Advanced Oxidation Processes (AOP) for Water Purification and Recovery. *Catal. Today* **1999**, *53*, 51−59.

(7) Zhao, Y. X.; Phuntsho, S.; Gao, B. Y.; Huang, X.; Qi, Q. B.; Yue, Q. Y.; Wang, Y.; Kim, J. H.; Shon, H. K. Preparation and Characterization of Novel Polytitanium Tetrachloride Coagulant for Water Purification. *Environ. Sci. Technol.* **2013**, *47*, 12966−12975.

(8) Samuel, M. S.; Shah, S. S.; Bhattacharya, J.; Subramaniam, K.; Pradeep Singh, N. D. Adsorption of Pb(II) from Aqueous Solution Using a Magnetic Chitosan/Graphene Oxide Composite and Its Toxicity Studies. *Int. J. Biol. Macromol.* **2018**, *115*, 1142−1150.

(9) Fathima, J. B.; Pugazhendhi, A.; Oves, M.; Venis, R. Synthesis of Eco-Friendly Copper Nanoparticles for Augmentation of Catalytic Degradation of Organic Dyes. *J. Mol. Liq.* **2018**, *260*, 1−8.

(10) Ikram, M.; Inayat, T.; Haider, A.; Ul-Hamid, A.; Haider, J.; Nabgan, W.; Saeed, A.; Shahbaz, A.; Hayat, S.; Ul-Ain, K.; Butt, A. R. Graphene Oxide-Doped MgO Nanostructures for Highly Efficient Dye Degradation and Bactericidal Action. *Nanoscale Res. Lett.* **2021**, *16*, 56.

(11) Kawashima, A.; Matsubara, K.; Honda, K. Acceleration of Catalytic Activity of Calcium Oxide for Biodiesel Production. *Bioresour. Technol.* **2009**, *100*, 696−700.

(12) Osuntokun, J.; Onwudiwe, D. C.; Ebenso, E. E. Aqueous Extract of Broccoli Mediated Synthesis of CaO Nanoparticles and Its Application in the Photocatalytic Degradation of Bromocrescol Green. 2018, *12* (7), 888−894, DOI: 10.1049/iet-nbt.2017.0277.

(13) Sadeghi, M.; Husseini, M. H. A Novel Method for the Synthesis of CaO Nanoparticle for the Decomposition of Sulfurous Pollutant. 2013, *49* (7), 39−49.

(14) Nithya, A.; Mohan, S. C.; Jeganathan, K.; Jothivenkatachalam, K. A Potential Photocatalytic , Antimicrobial and Anticancer Activity of Chitosan. *Int. J. Biol. Macromol.* **2017**, *104*, 1774−1782.

(15) Khan, A.; Goepel, M.; Colmenares, J. C.; Gla, R. Chitosan-Based N-Doped Carbon Materials for Electrocatalytic and Photocatalytic Applications. *ACS Sustainable Chem. Eng.* **2020**, *8*, 4708−4727.

(16) Karthikeyan, K. T.; Nithya, A.; Jothivenkatachalam, K. Photocatalytic and Antimicrobial Activities of Chitosan-$TiO_2$ Nanocomposite. *Int. J. Biol. Macromol.* **2017**, *104*, 1762−1773.

(17) Prokhorov, E.; Luna, B. G. Chitosan-ZnO Nanocomposites Assessed by Dielectric, Mechanical, and Piezoelectric Properties, polymers. *Polymers* **2020**, *12*, 1991.

(18) Li, F. B.; Li, X. Z.; Hou, M. F. Photocatalytic Degradation of 2-Mercaptobenzothiazole in Aqueous $La_3^+ - TiO_2$ Suspension for Odor Control. *Appl. Chem. B.* **2004**, *48*, 185−194.

(19) Anandan, S.; Vinu, A.; Lovely, K. L.; Gokulakrishnan, N.; Srinivasu, P.; Mori, T.; Murugesan, V.; Sivamurugan, V.; Ariga, K. Photocatalytic Activity of La-Doped ZnO for the Degradation of Monocrotophos in Aqueous Suspension. *J. Mol. Catal. B.* **2007**, *266*, 149−157.

(20) Nesic, J.; Manojlovic, D. D.; Andelkovic, I.; Dojcinovic, B. P.; Vulic, P. J.; Krstic, J.; Roglic, G. M. Preparation, Characterization and Photocatalytic Activity of Lanthanum and Vanadium Co-Doped Mesoporous $TiO_2$ for Azo-Dye Degradation. *J. Mol. Catal. A: Chem.* **2013**, *378*, 67−75.

(21) Toe, A. T.; Colpani, G. L.; Padoin, N.; Antonio, M.; Soares, C. Lanthanum Doped Titania Decorated with Silver Plasmonic Nanoparticles with Enhanced Photocatalytic Activity under UV-Visible Light. *Appl. Surf. Sci.* **2018**, *441*, 1057−1051.

(22) Rafiq, A.; Imran, M.; Ikram, M.; Naz, M.; Aqeel, M.; Ali, S. Photocatalytic and Catalytic Degradation of Organic Dye by Uncapped and Capped ZnS Quantum dots. *Mater. Res. Express* **2019**, *6*, 55801.

(23) Qumar, U.; Ikram, M.; Imran, M.; Haider, A.; Ul-Hamid, A.; Haider, J.; Riaz, K. N.; Ali, S. Synergistic Effect of Bi-Doped Exfoliated MoS2 Nanosheets on Their Bactericidal and Dye Degradation Potential. *Dalton Trans.* **2020**, *49*, 5362−5377.

(24) Seefeld, M. A.; Miller, W. H.; Newlander, K. A.; Burgess, W. J.; DeWolf, W. E.; Elkins, P. A.; Head, M. S.; Jakas, D. R.; Janson, C. A.; Keller, P. M.; Manley, P. J.; Moore, T. D.; Payne, D. J.; Pearson, S.; Polizzi, B. J.; Qiu, X.; Rittenhouse, S. F.; Uzinskas, I. N.; Wallis, N. G.; Huffman, W. F. Indole Naphthyridinones as Inhibitors of Bacterial Enoyl-ACP Reductases FabI and FabK. *J. Med. Chem.* **2003**, *46*, 1627−1635.

(25) Fage, C. D.; Lathouwers, T.; Vanmeert, M.; Gao, L. J.; Vrancken, K.; Lammens, E. M.; Weir, A. N. M.; Degroote, R.; Cuppens, H.; Kosol, S.; Simpson, T. J.; Crump, M. P.; Willis, C. L.; Herdewijn, P.; Lescrinier, E.; Lavigne, R.; Anné, J.; Masschelein, J. The Kalimantacin Polyketide Antibiotics Inhibit Fatty Acid Biosynthesis in Staphylococcus Aureus by Targeting the Enoyl-Acyl Carrier Protein Binding Site of FabI. *Angew. Chem., Int. Ed.* **2020**, *59*, 10549−10556.

(26) Abagyan, R.; Totrov, M. Biased Probability Monte Carlo Conformational Searches and Electrostatic Calculations for Peptides and Proteins. *J. Mol. Biol.* **1994**, *235*, 983−1002.

(27) Sinha, S.; Kr, A.; Kr, R.; Kr, N.; Shivani, K. Calcium Oxide ( CaO ) Nanomaterial ( Kukutanda Twak Bhasma ) from Egg Shell : Green Synthesis , Physical Properties and Antimicrobial Behaviour. Gre. *Mater. Today Proc.* **2020**, *43*, 3414−3419.

(28) Aziz, S. B.; Abidin, Z. H. Z.; Kadir, M. F. Z. Innovative Method to Avoid the Reduction of Silver to Silver Nanoparticles À + Ions Á Ag → Ag 1 in Silver Ion Conducting Based Polymer Electrolytes. *Phys. Scr.* **2015**, *90*, 35808.

(29) Thomas, R.; Mathavan, T.; Jothirajan, M. A.; Somaily, H. H.; Zahran, H. Y.; Yahia, I. S. An Effect of Lanthanum Doping on Physical Characteristics of FTO Thin Films Coated by Nebulizer Spray Pyrolysis Technique. *Opt. Mater.* **2020**, *99*, No. 109518.

(30) Roy, A.; Bhattacharya, J. Microwave-Assisted Synthesis and Characterization of CaO Nanoparticles. *Int. J. Nanosci.* **2012**, *10*, 413−418.

(31) Rodriguez, M. E. Characterization of Calcium Carbonate , Calcium Oxide , and Calcium hydrooxide as starting point to the improvement of line for their use in constraction. *J. Mater. Civ. Eng.* **2009**, *21*, 694−698.

(32) Magesan, P.; Sanuja, S.; Umapathy, M. J. Novel Hybrid Chitosan Blended $MoO_3$−$TiO_2$ Nanocomposite Film: Evaluation of Its Solar Light Photocatalytic and Antibacterial Activities. *RSC Adv.* **2015**, *5*, 42506−42515.

(33) Ram, K.; Mahara, J.; Ponpandi, R.; Chinnasamy, M.; Kumar, A. Hydroxyl Radical Scavenging Activity of $La_2$ $O_3$ Nanoparticles. *Phar. Innov. J.* **2019**, *8*, 759−763.



https://doi.org/10.1021/acsomega.2c02790
*ACS Omega* 2022, 7, 28459−28470

(34) Butt, A. R.; Ejaz, S.; Baron, J. C.; Ikram, M.; Ali, S.; Applications, S. CaO Nanoparticles as a Potential Drug Delivery Agent For Biomedical Applications. *Dig. J. Nanomater. Biostructures* **2015**, *10*, 799−809.
(35) Khanh, D.; Van On, V.; Hoat, D. M.; Rivas-silva, J. F.; Cocoletzi, G. H. Structural , Electronic , Magnetic and Optical Properties of CaO Induced by Oxygen Incorporation Effects : A First-Principles Study. *Phys. Lett. A* **2021**, *397*, No. 127241.
(36) Saiganesh, S.; Krishnan, T.; Narasimha, G.; Almoallim, H. S.; Prabhakar, V. Phytosynthetic Fabrication of Lanthanum Ion-Doped Nickel. *Crystals* **2021**, *11*, 124.
(37) Xiao, Q.; Zhang, J.; Xiao, C.; Tan, X. Photocatalytic Decolorization of Methylene Blue over Zn 1 − x Co x O under Visible Light Irradiation. *Mater. Sci. Eng., B* **2007**, *142*, 121−125.
(38) Liqiang, J.; Yichun, Q.; Baiqi, W.; Shudan, L.; Baojiang, J.; Libin, Y.; Wei, F.; Honggang, F.; Jiazhong, S. Review of Photoluminescence Performance of Nano-Sized Semiconductor Materials and Its Relationships with Photocatalytic Activity. *Sol. Eng. Mater.* **2006**, *90*, 1773−1787.
(39) Shaheen, S.; Iqbal, A.; Ikram, M.; Ul-Ain, K.; Naz, S.; Ul-Hamid, A.; Shahzadi, A.; Haider, A.; Nabgan, W.; Haider, J. Effective Disposal of Methylene Blue and Bactericidal Benefits of Using GO-Doped $MnO_2$Nanorods Synthesized through One-Pot Synthesis. *ACS Omega* **2021**, *6*, 24866−24878.
(40) Manikandan1, A. Manikandan1, Rare Earth Element (REE) Lanthanum Doped Zinc Oxide (La: ZnO) Nanomaterials: Synthesis Structural Optical and Antibacterial Studies. *J. Alloys Compd.* **2017**, *723*, 1155−1161.
(41) Rojas, J. V.; Toro, M.; Molina, M. C.; Castano, C. E. Facile Radiolytic Synthesis of Ruthenium Nanoparticles on Graphene Oxide and Carbon Nanotubes. *Mater. Sci. Eng., B* **2016**, *205*, 28−35.
(42) Liu, J.; Liu, M.; Chen, S.; Wang, B.; Chen, J.; Yang, D.; Zhang, S.; Du, W. Conversion of Au ( III ) -Polluted Waste Eggshell into Functional CaO/Au Nanocatalyst for Biodiesel Production. *Green Energy Environ.* **2020**, *7*, 352−359.
(43) Carvalho, F. L. S.; Asencios, Y. J. O.; Rego, A. M. B.; Assaf, E. M. General Hydrogen Production by Steam Reforming of Ethanol over $Co_3O_4/La_2O_3/CeO_2$ Catalysts Synthesized by One-Step Polymerization Method. *Appl. Catal., A* **2014**, *483*, 52−62.
(44) Hans, M.; Támara, J. C.; Mathews, S.; Bax, B.; Hegetschweiler, A.; Kautenburger, R.; Solioz, M.; Mücklich, F. Laser Cladding of Stainless Steel with a Copper-Silver Alloy to Generate Surfaces of High Antimicrobial Activity. *Appl. Surf. Sci.* **2014**, *320*, 195−199.
(45) Ruparelia, J. P.; Chatterjee, A. K.; Duttagupta, S. P.; Mukherji, S. Strain Specificity in Antimicrobial Activity of Silver and Copper Nanoparticles. *Acta Biomater.* **2008**, *4*, 707−716.
(46) Fang, W.; Chaofa, X.; Zheng, J.; Chen, G.; Jiang, K. Fabrication of Cu-Ag Bimetal Nanotube-Based Copper Silicates for Enhancement of Antibacterial Activities. *RSC Adv.* **2015**, *5*, 39612−39619.
(47) Haider, A.; Ijaz, M.; Imran, M.; Naz, M.; Majeed, H.; Khan, J. A.; Ali, M. M.; Ikram, M. Enhanced Bactericidal Action and Dye Degradation of Spicy Roots' Extract-Incorporated Fine-Tuned Metal Oxide Nanoparticles. *Appl. Nanosci.* **2020**, *10*, 1095−1104.
(48) Arshad, A.; Iqbal, J.; Mansoor, Q. NiO-Nanoflakes Grafted Graphene: An Excellent Photocatalyst and a Novel Nanomaterial for Achieving Complete Pathogen Control. *Nanoscale* **2017**, *9*, 16321−16328.
(49) Rock, O. C.; Heath, J. J. Fatty Acid Biosynthesis as a Target for Novel Antibacterials. *Curr Opin Investig Drugs.* **2014**, *23*, 146−153.
(50) Balemans, W.; Lounis, N.; Gilissen, R.; Guillemont, J.; Simmen, K.; Andries, K.; Koul, A. Essentiality of FASII Pathway for Staphylococcus Aureus. *Nature* **2010**, *463*, E3.
(51) Issaabadi, Z.; Nasrollahzadeh, M.; Sajadi, S. M. Green Synthesis of the Copper Nanoparticles Supported on Bentonite and Investigation of Its Catalytic Activity. *J. Cleaner Prod.* **2017**, *142*, 3584−3591.
(52) Isono, R.; Yoshimura, T.; Esumi, K. Preparation of $Au/TiO_2$ nanocomposites and their catalytic activity for DPPH radical scavenging reaction. *J. Colloid Interface Sci.* **2005**, *288*, 177−183.
(53) Morsella, M.; Alessandro, N.; Lanterna, A. E.; Scaiano, J. C. Improving the sunscreen properties of $TiO_2$ through an understanding of its catalytic properties. *ACS Omega* **2016**, *1*, 464−469.
(54) Huang, C. W.; Wu, M. C. Photocatalytic degradation of methylene blue by UV-assistant $TiO_2$ and natural sericite composites. *J. Chem. Technol. Biotechnol.* **2020**, *95*, 2715−2722.





https://doi.org/10.1021/acsomega.2c02790
*ACS Omega* 2022, 7, 28459−28470